

High Temperature Corrosive Environment in a Sintering Plant for Pig Iron Production and Its Effect on Different Steel Grades

Harald Rojacz,* Lubomir Krabac, Markus Varga, Karl Adam, and Günter Fafilek

The harsh environment in a sintering plant for pig iron production leads to high temperature corrosion of the sinter grates. In the present study, a detailed analysis of the corrosives in such applications is given to understand materials failure. Various steels are tested, revealing effects of various alloying concepts, the resulting phases and their corrosive behavior in this complex corrosive environment at ≈ 900 °C. In order to understand the underlying corrosion mechanisms, detailed analyses are performed. Results indicate mainly chlorine, sulfur, and oxidation based corrosive decay at elevated temperature and a high relevance of protecting alloying elements within the steels.

1. Introduction

The high temperature corrosion (HTC) is one of the most crucial effects responsible for downtime and maintenance costs in sintering plants for pig iron producing. Requirements on the materials for use in such applications involve not only wear resistance, but also excellent resistance against HTC and oxidation. Otherwise, utilized materials would be degraded by high-temperature oxidation processes causing failure and loss of operability. Therefore, the development of high temperature corrosion resistant steels used at elevated temperatures is of high scientific and industrial interest. In order to describe the underlying HTC mechanisms on materials and their degrading effects, it is crucial to investigate the surrounding atmosphere in the sintering plant.

Within a sintering plant for the pig iron production iron ore, coke, chalk, and other minor ingredients are mixed together and applied on a moving grate. This mixture is ignited within the ignition hood, where the temperature rises up to ≈ 900 °C. Subsequently, the sinter mixture is sintered together for the optimal use in a blast furnace.^[1,2]

During the sintering process, coke, lime, and various salts build a corrosive environment, which attacks the sinter grates causing various forms of corrosion. A detailed study of the corroding anions is crucial for understanding the mechanisms, which take place at the interactions of the utilized materials.

In order to understand the influence of the present corroding anions, five different heat and corrosion resistant steels from three steel classes, covering a broad spectrum of alloying concepts resisting these environments, have been chosen for investigation.^[3–6] The first steel class was represented by martensitic structure with low amount of Cr, showing high hardness and good oxidation resistance. The second steel class contained two steels of homogenous austenitic structure alloyed with Cr and Ni. This chemical resistant type of steel materials and coatings are expected to tend to uniform and intergranular corrosion and have good anti-corrosion features in similar corrosive environment.^[7–9] The steels of the third class were casted Cr-rich steels, with high amounts of precipitated Cr carbides. Those steels were predisposed for selective corrosion, due to various phases in one material, but show good wear behaviour.^[10–12]

Different corrosion mechanisms can occur within the sintering plant. Due to the presence of air in the wind boxes, high temperature oxidation is a crucial effect causing materials degradation. Chromia forming alloys tend to have a high resistance against oxidation,^[3–6,13,14] but the positive effects can be influenced to change for the even better, such as Y and Zr (even with applied inhibitors of their oxides,^[15–18] or can reduce those positive effects like Mo.^[19]

Due to the presence of coke, sulfur, and chlorine compounds can cause enhanced corrosion.^[3–6] This is caused by the dissolution of the formed oxides due to the

[*] H. Rojacz, L. Krabac, M. Varga
AC2T research GmbH, Viktor-Kaplan-Straße 2/C, 2700 Wiener Neustadt, Austria
Email: harald.rojacz@ac2t.at
K. Adam
voestalpine Stahl Linz GmbH, voestlpinne-Straße 1, 4020 Linz, Austria
G. Fafilek
Institute of Chemical Technologies and Analytics, Vienna University of Technology, Getreidemarkt 9, 1060 Vienna, Austria
G. Fafilek
CEST, Centre of Electrochemical Surface Technology GmbH, Viktor-Kaplan-Straße 2, 2700 Wiener Neustadt, Austria

DOI: 10.1002/srin.201600431

formation of chlorides, sulfates, and carbonates.^[20–26] This formation of corrosion products from oxidation layer educts is strongly influenced by the Gibbs free energy.^[27,28] The formation of different corrosion compounds is strongly influenced by the temperature and the present corrosive anions. Alkaline or acid high temperature corrosion can cause low melting eutectic systems, which can enhance corrosion.^[21,25,26]

The main objectives of this study are to investigate and understand the corroding atmosphere in the high temperature environment of a sintering plant for pig iron production. Several analytical techniques such as scanning electron microscopy (SEM), energy dispersive X-ray analysis (EDX), and X-ray diffraction (XRD) measurements have been carried out to investigate corrosives present in sintering plants. The corrosion resistance of various Cr-alloyed chemical and heat resistant steels at $\approx 900^\circ\text{C}$ has been examined and described. The investigations should show the corrosion resistance and -mechanisms of various steel-classes based on their alloying elements and the corrosive anions present in the atmosphere. Corrosion models should be evolved by intensive studies of the built-up corrosion products by SEM and EDX including EDX element mappings (EDXEM).

2. Experimental Section

2.1. Materials Investigated

Five heat resistant steel materials were investigated within the present research: one ferritic/martensitic steel, two conventionally heat-treated austenitic and chemical-resistant steels, and two ferritic steels with carbide precipitations, which are often in use because of their increased wear resistance.^[10–12] The chemical composition of all investigated materials is given in **Table 1**. Material A represents a martensitic steel with low amounts of alloying elements, such as Cr and Si. Austenitic Material B is a standard stainless steel containing 18 wt% Cr and

9.5 wt% Ni, comparable to Material C, which contains higher amounts of Ni, Mo, and Ti. Material D and E with high amounts of Cr and C precipitate carbides. Thereby, the influence of precipitations on the corrosion can be shown. Furthermore, the effect of the Cr amount within the Material D and E (18 wt% and 28 wt%, respectively), on the corrosion resistance can be pointed out.

2.2. Analyzing the Corrosives in Sintering Plants for Pig Iron Production

For the investigation of the underlying corrosion mechanisms, it is crucial to identify the corrosives present in the plant. Therefore, sinter ash was abstracted from the precipitator, as seen in **Figure 1a**. Stereo microscopy (SM, Olympus[®] SZX 16 equipped with camera Jenoptik Progres[®] C5) of the sinter ash was performed at a first shot. Afterward, to analyze various cations and anions present in the sintering ash, SEM-analyses supported by EDX-measurements were performed. To obtain more detailed results of corrosives, X-Ray diffraction (XRD) was performed.

2.3. High Temperature Corrosion Tests Simulating Sintering Plant Environment

2.3.1. Preparation of the Sintering Ash

The intention of this study was to investigate and correlate experimentally simulated HTC with sintering plant environment. To accelerate the simulation of the HTC in such environment, the water soluble salts were washed out of the collected sintering ash to recreate the harsh testing environment on the samples. Therefore 2 kg of sintering ash was washed out with 2 mL of distilled water under permanent stirring for 2 days. Afterward, the sintering ash was filtered from the solution and dried in the compartment drier. The remaining soluble salts were ground to engage the optimal miscibility with the sintering ash. Subsequently, the grounded salts were mixed together

Material		Alloying elements [wt%]							
<i>Pagination</i>	<i>DIN</i>	<i>Fe</i>	<i>C</i>	<i>Cr</i>	<i>Ni</i>	<i>Mn</i>	<i>Mo</i>	<i>Si</i>	<i>Ti</i>
<i>A</i>	1.0471	bal.	0.25	7	–	0.75	–	1.25	–
<i>B</i>	1.4301	bal.	0.07	18	9.5	0.75	–	–	–
<i>C</i>	1.4571	bal.	0.07	18	12	1.8	2.25	–	0.65
<i>D</i>	1.4743	bal.	1.6	18	0.8	0.75	0.4	1.25	–
<i>E</i>	1.4777	bal.	1.3	28	0.8	0.75	0.4	1.25	–

Table 1. Initial materials data.

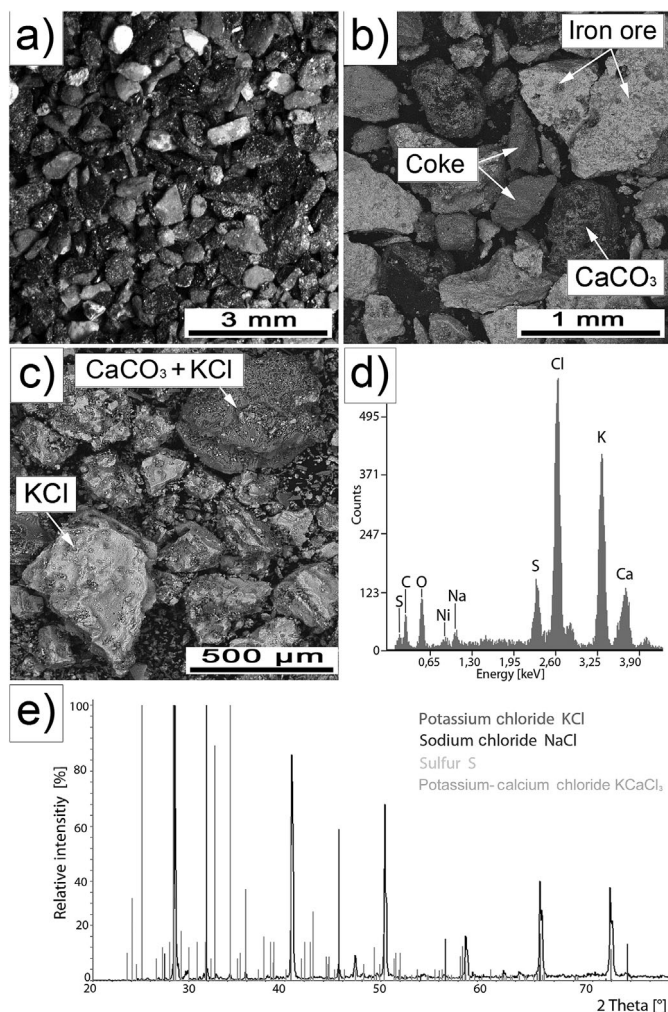


Figure 1. Overview on the precipitated sintering ash and the corrosives: a) stereo microscopy, b) SEM micrograph of the main phases, c) SEM micrograph of the dissolved corrosives present in the sintering ash, d) EDX-spectrum of the present corrosives, and e) XRD-pattern of the present corrosives.

with the unhandled sintering ash in the mass ratio of 1:10 to provide an appropriate and controlled environment for lab-scale testing.

2.3.2. Sample Preparation for HTC Testing

All samples were cut to dimensions of $8 \times 10 \times 15$ mm and finely ground to rectangular shape. The measurement of the real specimen dimensions was done using SM and micrometer. Both methods were of the same accuracy, while SM provided a more precise way of measuring the volume loss of the non-uniformly corroded test material.

2.3.3. Mass Loss Determination

In order to determine the mass loss during HTC testing, all samples were weighed before and after the lab tests. Therefore, the built-up corrosion products were removed mechanically (soft brushing and penetrating the less adhesive built-up layers) and chemically according to

the ASTM standard G1-03.^[29] The remaining inner denser oxidation layers were removed by a mixture of 100 ml of 65% HNO_3 and 900 ml of distilled water at 60°C in various etching cycles of a duration of 1 min each. After each etching cycle, the samples were mechanically cleaned and weighed. Cleaning cycles were repeated, until no more corrosion products could be found with SM at $7\times$ magnification. In order to exactly calculate the mass loss and the corrosion rates, the diagrams of dependency of the total mass loss on time of etching were built. The corrosion rate (CR) was determined according to the following equation:

$$CR = \frac{K \cdot \rho \cdot \Delta m}{A \cdot t} \quad (1)$$

where $K=10^4$ stands for a constant according to the standard, ρ [g m^{-2}] is the density of the investigated

material [g cm^{-2}], Δm [g] is the total mass loss due to corrosion, A [m^2] is the sample area as measured by SM and micrometre and t [h] stands for the corrosion time. CR is, therefore, given in [$\text{g m}^{-2} \text{h}^{-1}$].

2.3.4. High Temperature Corrosion Tests

High temperature corrosion tests were performed using four specimens of each material. Cleaned and weighed specimens were placed inside of two alumina crucibles, so each of them contained two specimens. In order to perform HTC tests, the crucibles were prepared with a 5 mm thick bottom layer of concentrated sintering ash. Subsequently, two specimens were placed into the crucible and fully covered with concentrated sintering ash. Finally, each crucible contained approximately 35 g of the sintering ash. Two crucibles were used in one test run. From the total amount of 4 specimens, one was intended for the metallographic cross section and three for statistically valid determination of the mass loss, volume loss, and corrosion rate.

The crucibles were given in the oven for 15 h at 900°C to simulate the maximum temperature reached by the sinter grates in the sintering plant. After the test cycle, specimens were cooled down to room temperature and the adherent sintering ash was removed from the built-up corrosion layers. First of all, the specimens' surfaces were examined using SM. Furthermore, the metallographic cross section of one specimen per material was prepared in order to explain the underlying mechanisms of HTC in sintering plant environment using optical microscopy (OM, Leica[®] MEF4 equipped with Leica[®] Microsystems camera) and high resolution SEM (Zeiss[®] Supra 40 VP) supported by EDX (EDAX[®] EDX Analysis System). The coarsest corrosion layers were removed from the surface of three remaining specimens, which were subsequently cleaned according to ASTM standard G1-03.^[29] Afterwards, they were weighed and the CR was calculated according to G1-03 standard.

3. Results and Discussion

3.1. Microstructural Characterization of Tested Materials

In the present study, five steel materials (Material A–E) were analyzed in order to evaluate their HTC behavior within the environment of the sintering plant. **Figure 2** demonstrates the microstructures of all tested materials as seen by OM. Material A (Figure 2a), a low Cr-alloyed casting steel, shows a martensitic microstructure with small amounts of precipitated MnS_2 (black dots in the microstructure). Material B (Figure 2b) represents a standard chemical resistant steel of a homogeneous austenitic structure, with twin grain boundaries and an average grain size of $\approx 20 \mu\text{m}$. Material C (Figure 2c), a heat- and chemical-resistant steel, shows austenitic

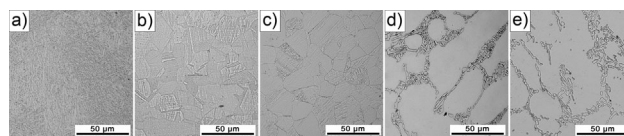


Figure 2. Microstructural analysis of the materials investigated: a) martensitic Material A – 1.4710, b) austenitic Material B – 1.4301, c) austenitic Material C – 1.4571, d) ferritic-carbide Material D – 1.4743, and e) ferritic-carbide Material E – 1.4777.

microstructure with an average grain size of $\approx 22 \mu\text{m}$. Material D (Figure 2d), a Cr-alloyed and heat-resistant steel with ferritic matrix, contains primary Cr-carbides of Cr_7C_3 structure.^[30] Black dots visible on Figure 2d are mostly oxide inclusions formed during the casting process. Material E (Figure 2e), a heat resistant and highly Cr-alloyed steel of ferritic matrix, contains also primary Cr-carbides, such as Material D.

3.2. Corrosive Environment in a Sintering Plant for Pig Iron Production

As seen in Figure 1a, the SM of the sintering mixture, represented by the sinter ash, shows three main phases: iron ore, coke, and lime. The SEM images of the sintering ash with the identified phases can be seen in Figure 1b. A more detailed analysis of the corrosive salts with SEM can be seen in Figure 1c, pointing out various potassium chlorides and lime as corrosives. The EDX-spectrum of the water soluble corrosives of the sintering ash is given in Figure 1d, where the main corrosives are KCl, NaCl, and CaCO_3 , with sulfur/sulfides and a small amount of Ni salts. In the XRD-patterns (Figure 1e), four main corrosives can be detected: KCl, NaCl, KCaCl_3 , and sulfur. An overview on the present corrosives and their average amount in the sintering ash is given in **Table 2**.

The chemical composition of the corrosives was determined at room temperature. Due to the corrosives found within the sintering plant environment, the used materials should be resistant against the following forms of corrosion: i) oxidation, due to the amount of oxygen in the drawn air and the high temperature;^[4,6,20,31] ii) metal dusting, as a severe form of corrosion at elevated temperatures, formed by saturated carbonaceous environments^[32–34]; iii) HTC due to the salt deposits formed by the presence of corroding anions at the boundary layer between the sinter and the sinter grate.^[4,6,21–27,31] This type of corrosion forms thick deposits, which can spall off, and is highly critical due to the formation of liquid eutectics at the boundary layer between corrosion products and the base metal. The liquid eutectics show high ability to migrate, therefore, can cause huge decay.^[26,35,36] Furthermore, vaporized and volatile salt mixtures and their products of decomposition, together with a mixture containing corroding gases or

Corrosive	Average amount [wt%]
Potassium Chloride KCl	4–5
Sodium Chloride NaCl	~1
Potassium-Calcium Chloride $KCaCl_3$	~1
Calcium Carbonate $CaCO_3$	~25
Sulfur S	3–4
Carbon C	~25

Table 2. Corrosive content of the sintering ash.

condensates can easily migrate and desublimates/condensate on various spots, which can lead to further, enhanced, decay.^[21,37–39]

Due to the high amount of various corrosive salts present in the sinter mixture, other salts, such as K_2SO_4 can be formed and the HTC behavior of the materials can be affected subsequently.^[40] In Cr-rich steels, K_2SO_4 tends to be less corrosive on the formed Cr oxide scales.^[41] The formation of Na_2SO_4 from NaCl can also occur to enable the HTC Type 1 to take place at $\approx 900^\circ C$, which means that molten salts penetrate throughout the oxide scales and dissolve them to form the other salts, mostly in presence of sulfur. Molten salts and their migration are mostly common throughout cracks and pores, but they can also migrate to the boundary zone between base material and oxide scales due to active dissolution of oxides to chlorines or sulfates.^[42] Moreover, various forms of gases Cl, HCl, CO_2 , and SO_3 can be synthesized from of the present corrosives, which causes the gaseous corrosion of the samples, as well.^[40,43] In general, it can be said that various salts can form other corrosive salts at this temperatures due to the differences in the molar standard enthalpy of formation ΔH_f° .^[44,45] Furthermore, the presence of other chemical substances can also strongly affect the formed corrosion scales, which is strongly influenced by the Gibbs free energy of formation $\Delta_f G$.^[27,28]

3.3. High Temperature Corrosion Studies

In the following subsections, the effects of HTC in sintering plants for pig iron production on the investigated steels are outlined. Quantitative and qualitative analyses were performed, in order to understand the various mechanisms of HTC on the materials. Furthermore, to quantitatively describe the corrosion resistance of the materials, corrosion rates CR were calculated from experimentally obtained mass losses. In order to reveal the corrosion scale structure and subsequently determine the corrosion models for various steel classes, SEM analyses were performed.

3.3.1. Corrosion Rates of the Materials Investigated

Figure 3 shows the corrosion rate (CR) calculated, according to Equation 1. As seen in the figure, higher concentration of Cr and other stabilizing elements can decrease the corrosion rate. However, higher amounts of alloying elements do not always increase the stability against corrosion, as seen in the chart. Considering two steel classes, (i) both chemical resistant austenitic steels (material B and C), and (ii) Cr-rich ferritic-carbide steels (material D and E), the higher alloyed steels tend to corrode more. For the austenitic steels, material B corrodes less than the material C with a higher alloying content. This finding indicates a negative effect of Ni, present in a higher alloying content. This phenomena can be also observed in case of ferritic-carbide steels. Material D, with an alloying content of about 23 wt% is more stable against corrosion than the material E with 32.5 wt% of the alloyed elements (mainly Cr). This can be ascribed to the higher ability of the steel material to form the protective layers at higher alloying content. On the other hand, due to oxidation and corrosion, the higher content of alloying elements does not provide better protection against the penetration by the corrosives KCl and sulfur, throughout the faults within the surface layer. Moreover, the corrosion can be enhanced by the presence of other alloying elements.^[15,21–23] The limitation of the corrosion protection of chromia combined with elements, such as Ni- and Mn-oxides is even more pronounced if higher alloying contents are present (Material C and E).

3.3.2. SEM-EDX Analyses of Formed Corrosion Scales

The protective properties of the corrosion and oxidation products at elevated temperatures strongly depend on the material's chemical composition and the corrosive anions present at the exposed surface.^[3–5]

As seen in for Material A in Figure 4a, large and porous corrosion scales (≈ 2.5 mm) are formed on the surface due to the low amounts of stabilizing elements^[8] and materials degradation. The dominant corrosion mechanism is a

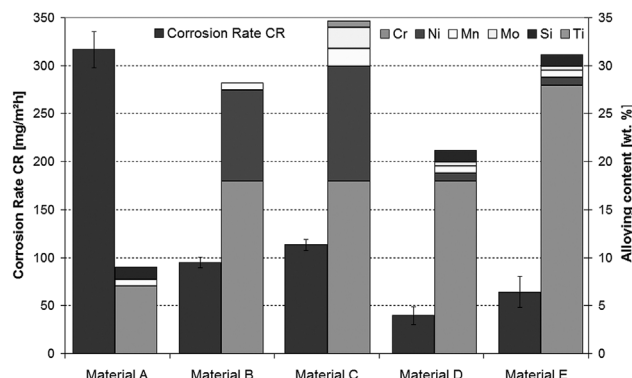


Figure 3. Percentage volumetric loss and corrosion rates (CR) of the materials investigated.

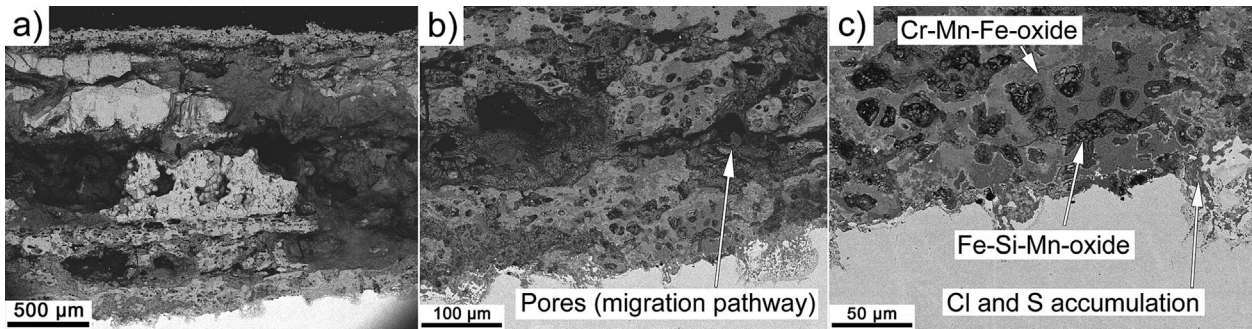


Figure 4. SEM images of adherent corrosion layers and their consistence on Material A.

uniform corrosion caused by the present corrosives, such as KCl, NaCl, and S, and promoted by a homogenous microstructure of the material. Figure 4b points out porous Fe–Cr mixed oxides enabling a good corrosives migration to the sparsely protected metal surface. Figure 4c depicts spongy Cr–Mn–Fe oxides with parts of Fe-rich mixed oxides. Moreover, the molten salt corrosion leads to a local decay of the metal matrix due to the previous Cl and S accumulation. In the zones with no protective oxide scales, the molten salts can corrode into the base material unimpededly. The EDX element mapping (Figure 5)

indicates the distribution of cations and anions present in Material A. The brighter the area within the picture, the more counts were measured from a certain element. The outward of the scale contains an adherent layer of sinter mixture, represented by the high amount of Ca. The outer oxide scale consists predominantly of Fe oxides Fe_xO_y with parts of mixed Fe–Mn oxides $Fe_xMn_yO_z$ and chlorides. Due to the formation of gaseous components within the sinter and due to the low amounts of stabilizing elements, the scale is highly porous with pores of ≈ 1 mm in diameter, which enables an easy migration of corrosives. The inner

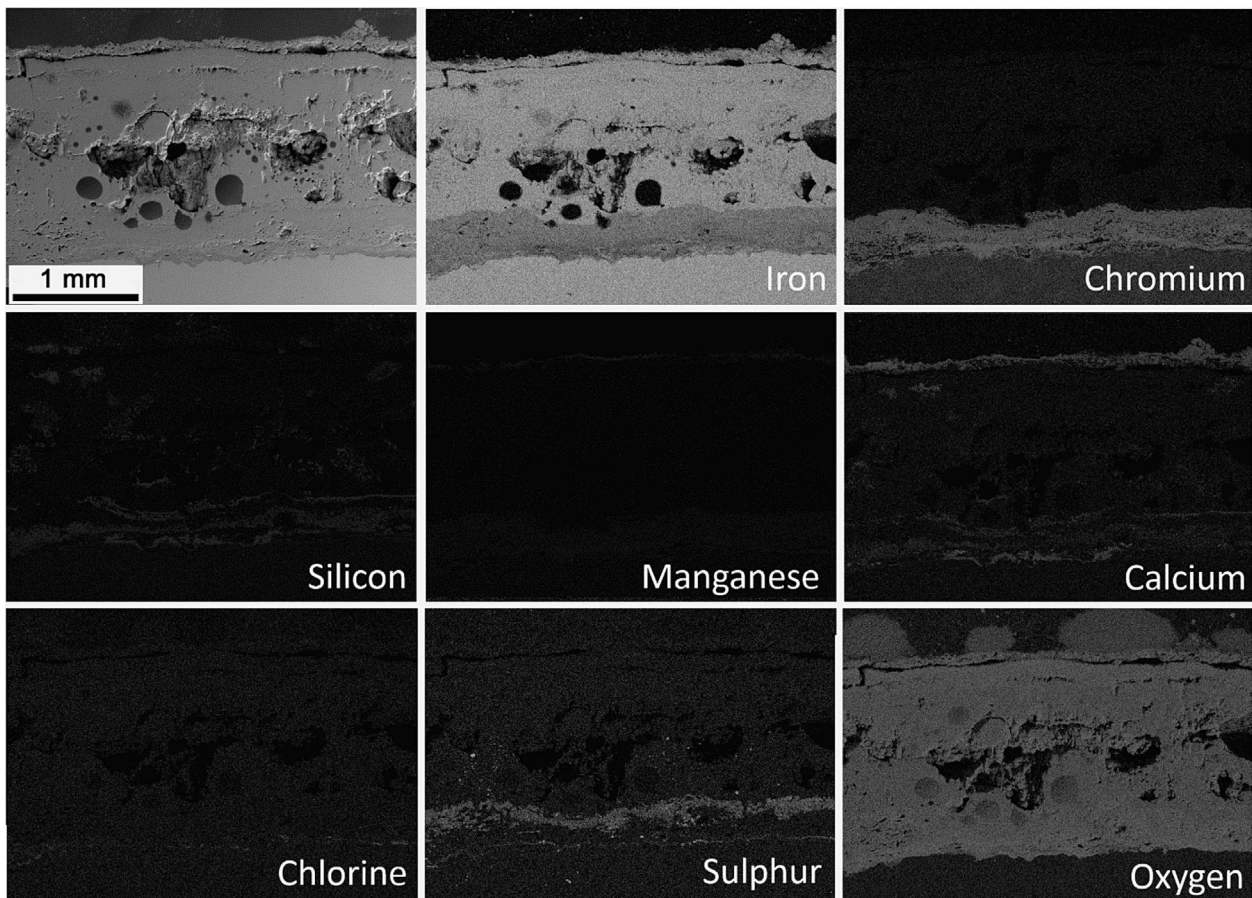


Figure 5. EDX mappings of various elements present at Material A after the HTC test.

oxide layer is Cr oxide-dominated and contains also Cr–Mn mixed oxides, such as Cr_2O_3 , Cr_3O_4 , and MnO_2 . Furthermore, sulfur can be found at the outer side, and SiO_2 and CaCO_3 at the inner side of this layer. The boundary between the oxide-type scales and the base material consists mostly of Fe and Cr mixed oxides with high amounts of sulfur at the outer border and chlorine at the inner border (Figure 5). At the diffusion layer between the scales and the base material, eutectics of sulfur and chlorine salts causes molten salt corrosion.

Material B, an austenitic chemical resistant steel, forms adherent layers of about $300\ \mu\text{m}$ in thickness. SEM investigations (Figure 6a–c) point out a partial accumulation of corrosives at weak points within the scale.^[27]

In general, austenitic steels can partially suffer the uniform and partially intergranular corrosion. Moreover, the weakest spot for HTC to begin are grain boundaries, due to their varying concentrations of Cr and Ni throughout the grains causing the decay of the grain boundaries and subsequently of the whole grains.^[4,5] The decayed grains are, then, transfer into the diffusion layer, causing a corrosion scale formation. This as-formed boundary layer between the corrosion scale and the base metal ($\approx 20\ \mu\text{m}$) consists mainly of a mixture of corrosives.^[24,46,47]

Corrosion mechanisms of Material C are displayed in Figure 6d–f. Mixed oxide scales of $200\ \mu\text{m}$ thickness and more are formed due to the exposition of the material to the sinter atmosphere. The higher amount of alloying elements enables less porous oxide layers. Formation of Fe chlorides can be explained as the decomposition of NaCl and KCl, which results in synthesis of Na_2SO_4 and K_2SO_4

followed by reaction of chlorine with the present metals.^[48] It is worth noting, that the Ni distribution in higher alloyed austenitic steels differs from the distribution of this element in lower Ni alloyed austenitic steels.

As seen in the EDX mapping for this material (Figure 7), the outer oxide layer formed on austenitic steels contains Ni, but the main part remains in the boundary layer of the substrate. Due to that Ni-chlorides and sulfates, are formed by the aggressive free Cl^- , respectively, the SO_2 under concomitant oxidation (SO_3) from corroding salts.^[48,49] Due to the formation of sulfates and chlorides out of oxides and corroding anions, higher amounts of Ni are not mandatorily increasing the resistance against HTC. The inner oxide layer mainly consists of Cr–Mn mixed oxides with low amounts of chlorine. The diffusion layer at the border of base material and corrosion scale is dominated by chlorine and sulfur compounds like FeCl_3 , NiCl_2 , CrCl_2 or FeS , FeS_2 , NiS , MnS ,^[24,48,49] which can be decomposed to other components by releasing S and Cl.^[50]

Material D (Cr-alloyed ferritic-carbide steel – Figure 8a), which exploits an adherent corrosion scale of $\approx 200\ \mu\text{m}$. As seen in Figure 8b and c, the dominant corrosion mechanisms are uniform corrosion due to the present corrosive anions, while the carbides suffer from selective corrosion due to their less noble electrochemical potential compared to the Fe–Cr based matrix.^[14] This effect is accompanied by selective corrosion of the carbides enabling the deep penetration of corrosives into the base material, which is similar to Material E, as seen in Figure 8d–f. Corrosives accumulated on the base material surface cause a good migration ability throughout the leftover channels of the carbide network.

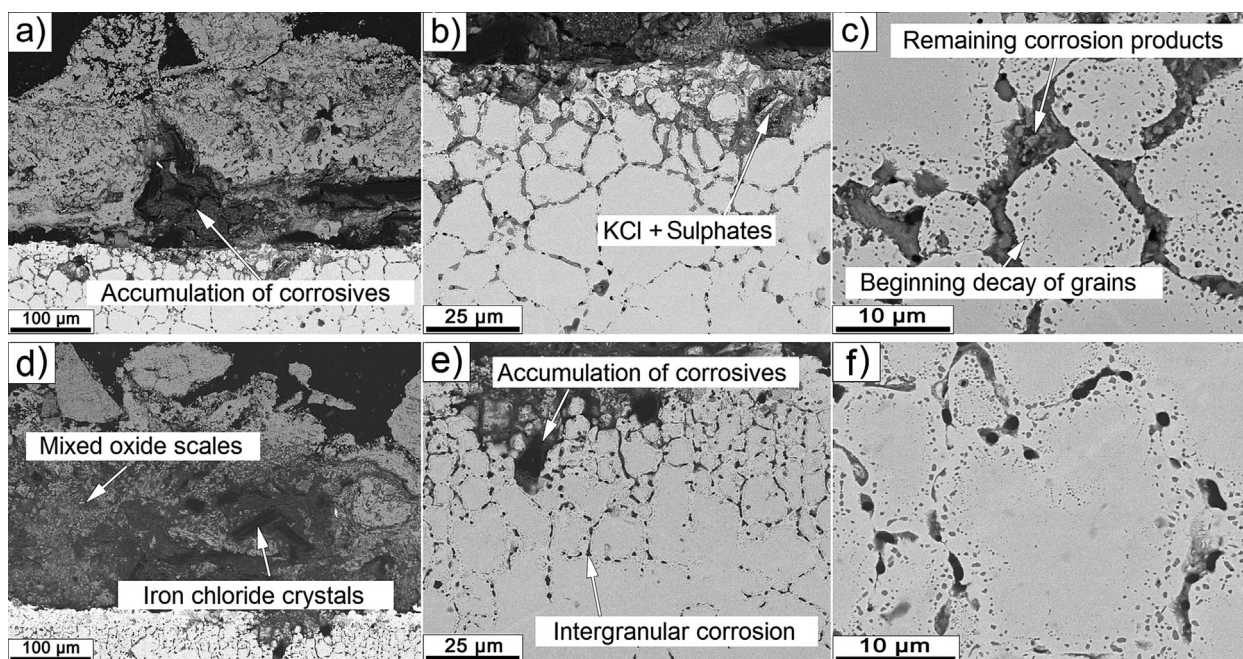


Figure 6. SEM images of adherent corrosion layers and their consistence on Material B a–c), and C d–f), representing austenitic steels.

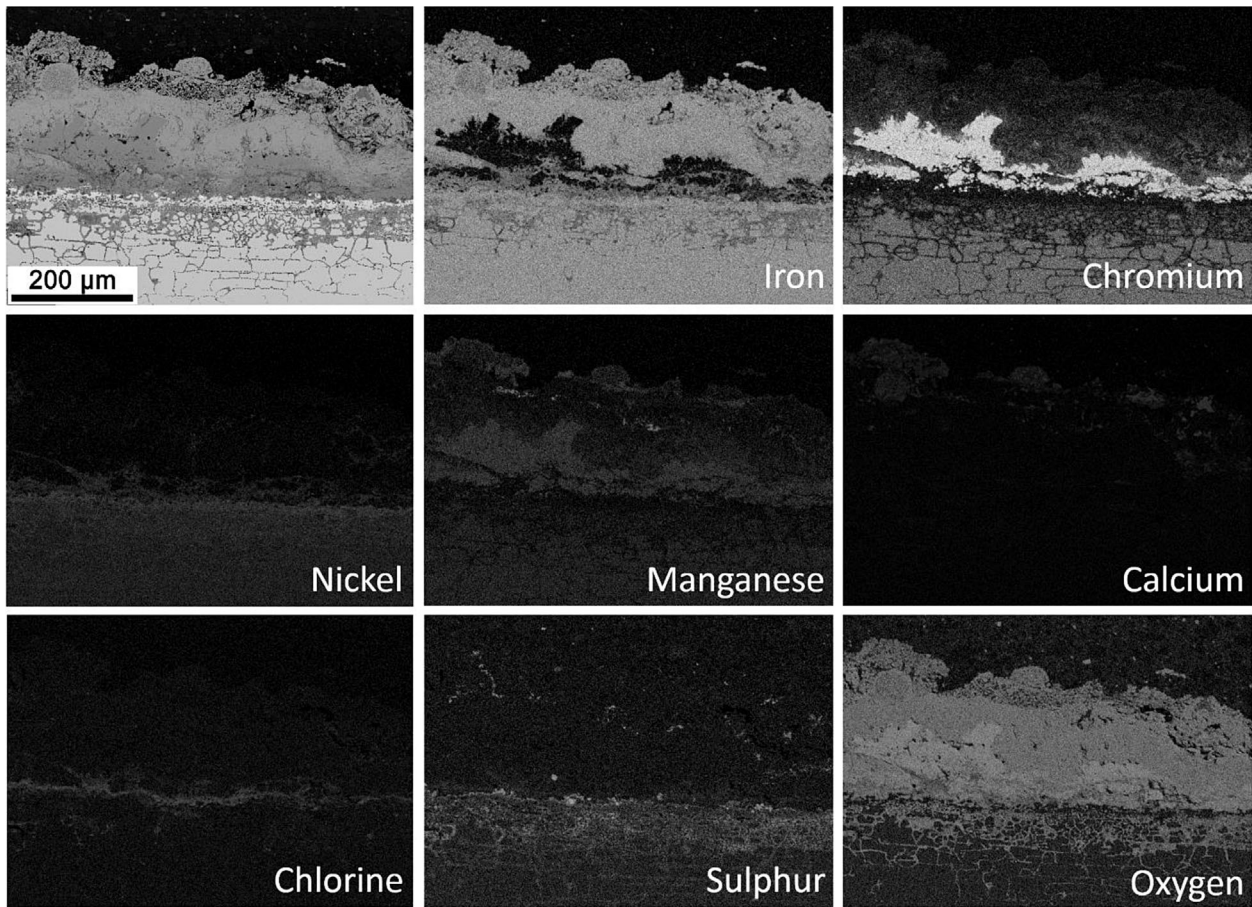


Figure 7. EDX mappings of various elements present at austenitic steels (Material C) after the HTC test.

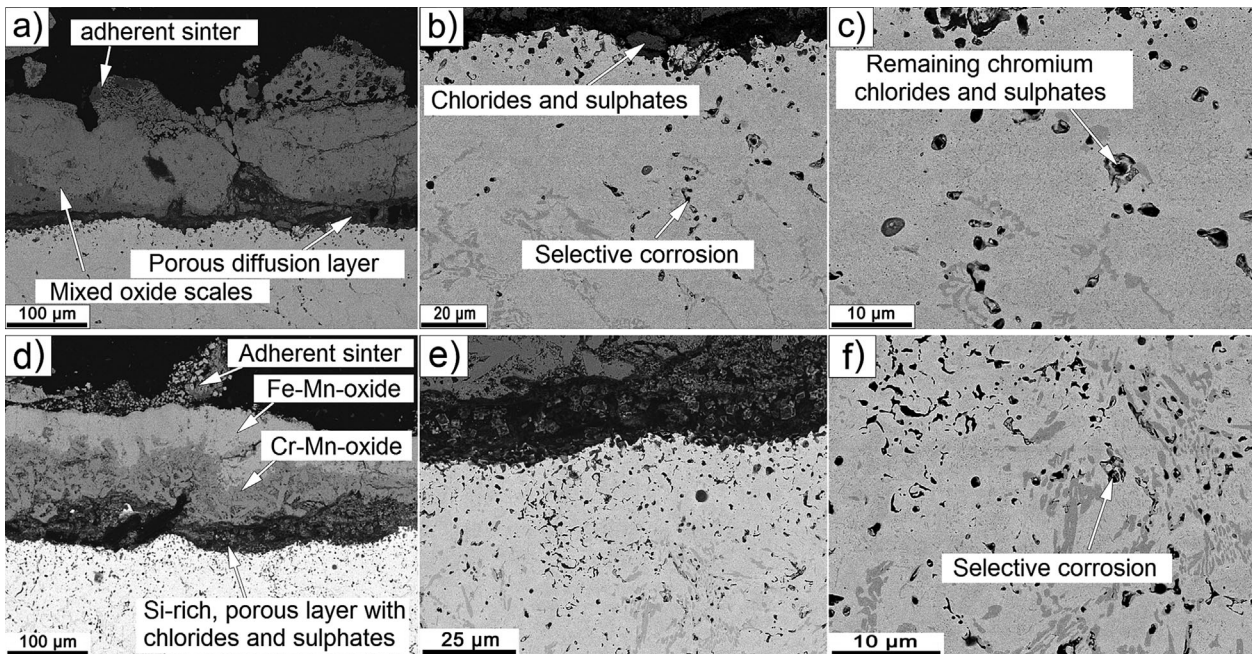


Figure 8. SEM images of adherent corrosion layers and their consistence on ferritic steels with chromium carbides: a–c) Materials D, d–f): Material E.

Elevated amounts of Cr result in a high ability to form Cr oxides, responsible for a high potential of Cr to diffuse to the sample's surface and for the concomitant molten salt corrosion in the diffusion layer. More Cr present at the surface at higher alloying contents enables a better oxy-chloridation of Cr and other mixed oxide scales formed, which increases the corrosion rates. Due to these processes, Material E is more corroded than Material D, albeit Material D contains lower amounts of alloying elements.

EDX mappings on ferritic steels with chromium carbides (Figure 9) visualize adherent sinter ash chunks (mostly CaCO_3 or its decomposition products) (Figure 9 - Calcium). The outer layer of the oxide scale is dominated by Fe oxides with incorporated chlorides. On the surface, accumulations of sulfur can be detected in the regions of the sinter ash chunks, but due to the relatively dense surface, low amounts of sulfur can be detected in the inner scale regions. As seen in the Figure 9, chlorine penetrates through the scale which brings along Cl accumulations at the diffusion layer and various chemical compounds like FeCl_3 and $\text{CrCl}_2/\text{CrCl}_3$.^[48–50] At the inner oxide scale, mixed Cr–Mn oxides can be found, which are not densely packed with the diffusion layer. It can be said, that volatile compounds have been formed. Solid

compounds which were formed during the corrosion process mainly consist of SiO_2 mixed with chlorine salts, with parts of sulfur compounds, which are evenly distributed in low concentration. Adherent sinter can be found at the outer oxide scales consisted of Fe oxides of the type Fe_xO_y with parts of mixed Fe–Mn oxides ($\text{Fe}_x\text{Mn}_y\text{O}_z$) and chlorides. Only few cracks and pores are formed due to the high amount of Cr, which enables a comparatively highly dense layer. The inner oxide scale is built of Cr–Mn mixed oxides. The diffusion layer at the border between corrosion scales and base material is composed mainly of SiO_2 with amounts of accumulated Cl and S causing uniform molten salt corrosion of the matrix, as previously stated.

3.3.3. Chemical Reactions During High Temperature Corrosive Processes

In general, it is well-known that the material loss due to HTC is more severe, when the temperature of reaction system is higher than the melting point of deposits.^[51] In this study, the melting point of the corrosive salt surrounding the specimens in ceramic crucibles was experimentally determined to be in the range of $\approx 590\text{--}710\text{ }^\circ\text{C}$, which is lower than the testing temperature

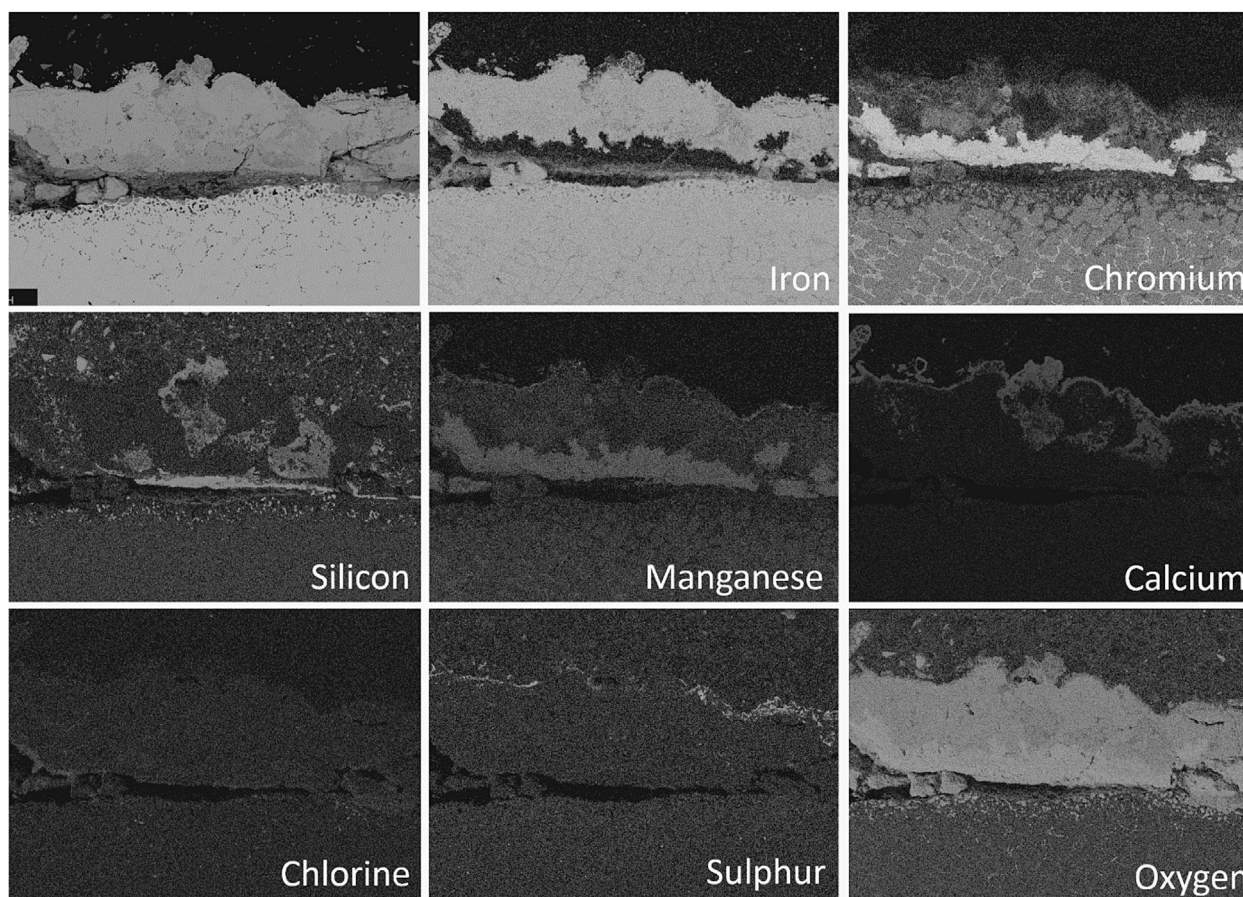


Figure 9. EDX mappings of various elements present at Material D after the HTC tests, representing ferritic steels with chromium carbides.

($\approx 900^\circ\text{C}$). Due to this fact, it can be expected, that the molten phase is formed and increases the corrosion.

The chain of reactions taking place during the HTC is initiated by the oxychloridation of metals, as previously described by Tsaur et al.^[51] In this step, NaCl and KCl from the molten salt react with oxygen and forms sodium- and potassium-containing oxides and chlorine. Further, the chlorine is either released to the atmosphere and subsequently removed from the reaction system, or dissolved into the metal oxide lattice increasing the alloy's oxidation rate due to the increased content of cation vacancies.^[51] Based on the former studies,^[51–56] dealing with mechanisms of accelerated corrosion caused by molten salts composed mainly of NaCl and KCl, possible chemical reactions during HTC testing were proposed. In order to determine the possibility of such reactions, their Gibbs free energy changes at 1200 K ($\approx 927^\circ\text{C}$) were calculated using the published thermochemical data (see Table 3).^[57]

As demonstrated by thermodynamic data listed in Table 3, in the oxychloridation step, iron and chromium have higher tendency to react with NaCl than with KCl.

Moreover, at given temperature, the formation of NaFeO₂ is favored, while Na₂O or K₂O has less tendency to be formed; in general potassium is likely to react to sulfates from KCl in presence of sulfur containing chemical compounds.^[58]

Regarding the chloridation reaction, chromium has the greatest affinity to react with chlorine to form its chloride, while the driving force for the formation of nickel chloride is the lowest and, hence, will be left in the alloy substrate. This fact is demonstrated by Material B and C, respectively. Subsequently, the products of chloridation reactions, metal chlorides dissolved in molten salt, are evaporated or diffused as metal ions outward and react with oxygen to form a non-protective duplex-layer scales consisting of chromia at the inner and iron oxides at the outer scale, which is confirmed by the performed SEM analyses as given in Figure 5–9.

3.3.4. Physico-Chemical Discussion on Corrosion Mechanisms and Evolved Corrosion Models

The HTC of various steel materials in simulated corrosive environment of a sintering plant results in the formation of

Reactions	$\Delta G_{1200\text{K}}$ [kJ mol ⁻¹]
Oxychloridation of metals	
$1/2 \text{Cr (s)} + \text{O}_2 \text{(g)} + \text{NaCl (l)} = 1/2 \text{Na}_2\text{CrO}_4 \text{(l)} + 1/2 \text{Cl}_2 \text{(g)}$	-216
$1/2 \text{Cr (s)} + \text{O}_2 \text{(g)} + \text{KCl (l)} = 1/2 \text{K}_2\text{CrO}_4 \text{(s)} + 1/2 \text{Cl}_2 \text{(g)}$	-157
$2 \text{Fe (s)} + 2 \text{O}_2 \text{(g)} + 2 \text{NaCl (l)} = 2 \text{NaFeO}_2 \text{(s)} + \text{Cl}_2 \text{(g)}$	-300
$\text{Fe (s)} + \text{O}_2 \text{(g)} + \text{NaCl (l)} = 1/2 \text{Fe}_2\text{O}_3 \text{(s)} + 1/2 \text{Na}_2\text{O (s)} + 1/2 \text{Cl}_2 \text{(g)}$	-78
$\text{Fe (s)} + \text{O}_2 \text{(g)} + \text{KCl (l)} = 1/2 \text{Fe}_2\text{O}_3 \text{(s)} + 1/2 \text{K}_2\text{O (l)} + 1/2 \text{Cl}_2 \text{(g)}$	-30
Chloridation of metals	
$\text{Fe (s)} + \text{Cl}_2 \text{(g)} = \text{FeCl}_2 \text{(l)}$	-206
$2/3 \text{Fe (s)} + 3 \text{Cl}_2 \text{(g)} = 2/3 \text{FeCl}_3 \text{(g)}$	-152
$\text{Cr (s)} + \text{Cl}_2 \text{(g)} = \text{CrCl}_2 \text{(l)}$	-252
$2/3 \text{Cr (s)} + 3 \text{Cl}_2 \text{(g)} = 2/3 \text{CrCl}_3 \text{(g)}$	-193
$\text{Ni (s)} + \text{Cl}_2 \text{(g)} = \text{NiCl}_2 \text{(s)}$	-128
Oxidation of metal chlorides	
$2 \text{FeCl}_2 \text{(l)} + \text{O}_2 \text{(g)} = 2 \text{FeO (s)} + 2 \text{Cl}_2 \text{(g)}$	+23
$3/2 \text{FeCl}_2 \text{(l)} + \text{O}_2 \text{(g)} = 1/2 \text{Fe}_3\text{O}_4 \text{(s)} + 3/2 \text{Cl}_2 \text{(g)}$	-57
$4/3 \text{FeCl}_2 \text{(l)} + \text{O}_2 \text{(g)} = 2/3 \text{Fe}_2\text{O}_3 \text{(s)} + 4/3 \text{Cl}_2 \text{(g)}$	-66
$4/3 \text{FeCl}_3 \text{(g)} + \text{O}_2 \text{(g)} = 2/3 \text{Fe}_2\text{O}_3 \text{(s)} + 2 \text{Cl}_2 \text{(g)}$	-36
$4/3 \text{CrCl}_2 \text{(l)} + \text{O}_2 \text{(g)} = 2/3 \text{Cr}_2\text{O}_3 \text{(s)} + 4/3 \text{Cl}_2 \text{(g)}$	-214
$4/3 \text{CrCl}_3 \text{(s)} + \text{O}_2 \text{(g)} = 2/3 \text{Cr}_2\text{O}_3 \text{(s)} + 2 \text{Cl}_2 \text{(g)}$	-164
$2 \text{NiCl}_2 \text{(s)} + \text{O}_2 \text{(g)} = 2 \text{NiO (s)} + \text{Cl}_2 \text{(g)}$	-7

Table 3. Gibbs free energy change $\Delta_r G$ of selected reactions taking place in the reaction system at 1200 K ($\approx 927^\circ\text{C}$).⁵⁷

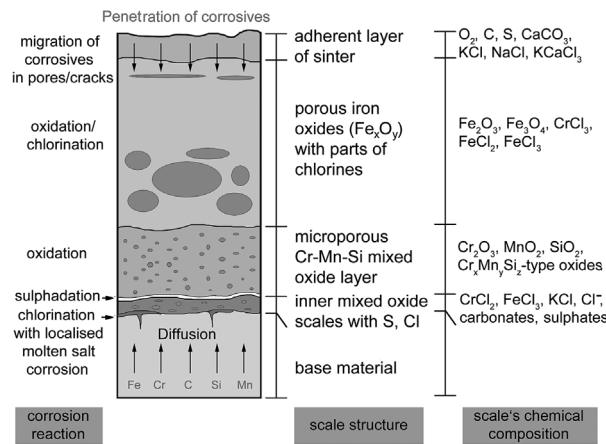
oxide scales consisting of an outer porous oxide layer and an inner Cr–Mn dominated oxide layer, as described in detail in Section 3.3.2.

Moreover, thermodynamic parameters, such as diffusion coefficient D and Gibbs free energy of formation $\Delta_f G$ were used to develop the corrosion models for predicting the corrosion rate of martensitic, austenitic and ferritic-carbide steels under harsh chemical conditions and high temperature. Cr with its high diffusion coefficient diffuses to the outside of the material and oxidize with the present oxygen, which diffuses inwards. The nuclei are formed in selective areas forming Cr and Fe oxides.^[4,6,17,18,59] Due to the high diffusion coefficient of Cr, a high amount of Cr is present on the samples surface causing the formation of dense chromite layers on the samples surface. Iron, due to its low self-diffusion coefficient can be found at the outer surface, due to the higher migration velocity in chromite. Manganese with a diffusion coefficient between Fe and Cr can be found regularly distributed at the whole scale. In the presence of Ni, various nuclei, like NiCr_2O_4 , FeCr_2O_4 or

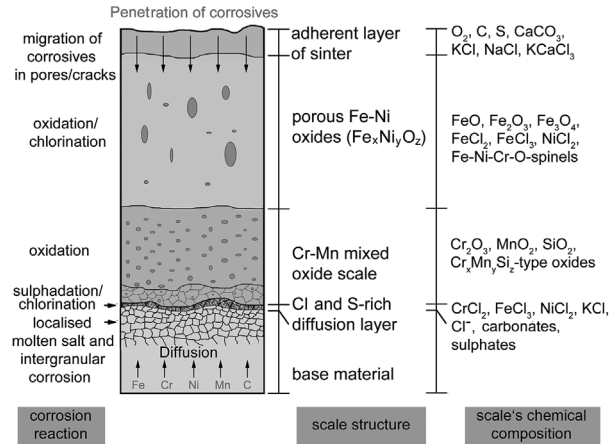
Fe–Ni spinel type oxides^[4,6,17,18] are formed. Due to its relatively high diffusion coefficient Fe–Ni mixed oxides can be found at the outer layer. Silicon, is only present in the boundary zone of the scales, due to the lowest D value, but enhances the diffusion of iron to outer scales.^[46]

Based on measured and calculated facts, and a correlation among various corrosive effects studied in this study and cited literature, corrosion models were developed for all tested materials and displayed in a schematic overview in Figure 10. As visible, the structure of corrosion scales is mostly oxide-based, represented by Fe_3O_4 , FeSiO_4 , Cr_3FeO_4 , NiCr_2O_4 , FeCr_2O_4 , Ni_2O_3 , Cr_2O_3 , Cr_3O_4 , and SiO_2 , which are vulnerable to an attack by chlorine-containing salts.^[17,18,57] The formed chlorides are mostly dominated by FeCl_3 , NiCl_2 , and the highly volatile SiCl_4 , possibly also by interstitially dissolved chlorine. Due to the presence of sulfur, the formation of sulfates, such as FeSO_4 and NiSO_4 , can be expected. Furthermore, the formation of liquid phase of FeO– Fe_2SiO_4 eutectic is possible to take place due to Si

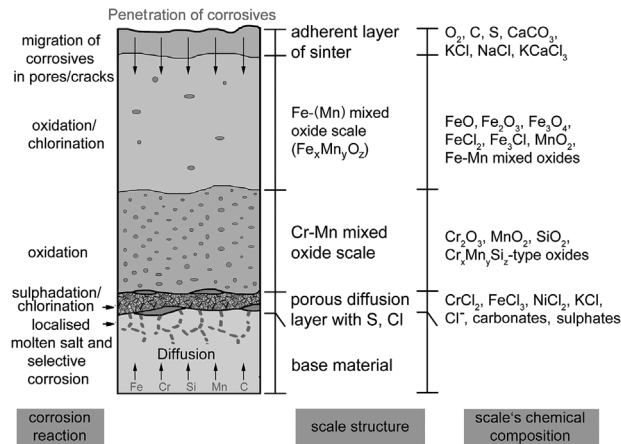
a) chromium alloyed martensitic steels



b) austenitic Cr-Ni-steels



c) chromium-rich ferritic-carbide steels



d) oxygen partial pressure progression

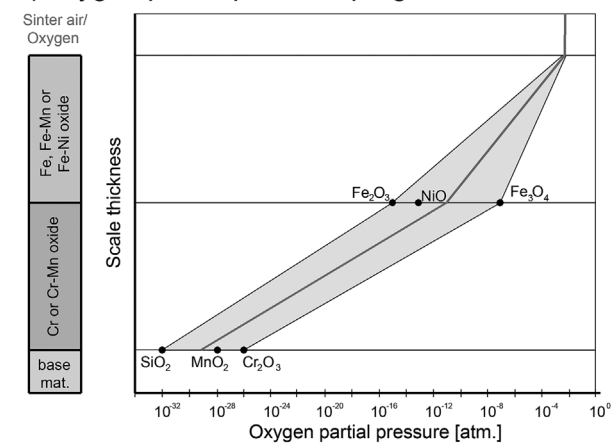


Figure 10. Corrosion models of the three steel classes investigated: a) martensitic Cr-steels, b) austenitic Cr-Ni-steels, and c) ferritic-carbide Cr-steels.

content in steel material, but Si generally increases the corrosion resistance in such environment.^[48]

Overall, the presented findings are consistent with EDX mappings of corrosion scales (Figure 5, 7, and 9) of the investigated materials as well as with the results of other studies.^[24,35–37,60]

Figure 10d points out the partial pressure progression of oxygen throughout the oxide scale. It can be stated, that different oxides can be formed even at very small oxygen partial pressures (Cr, Mn, Si) which lie inner than those with a tendency to higher partial pressures during their formation (Fe and Ni). Since NiO is located in the range between two formed iron oxides, no difference in the partial pressure progression is observed. Furthermore, Ni plays a subordinate role in the corrosion stability. On the other hand, slight changes can be seen in the presence of alloying elements, such as Si and Mn, which are beneficial for the corrosion resistance of Cr–Ni steels, also in combined corrosive attack like in sintering plants.

In summary, it can be said that HTC processes in sintering plants occur in the temperature range from 700 to 900 °C in the presence of sulfate potassium and chlorine salt deposits, such as Na₂SO₄, K₂SO₄, KCl, NaCl, and sulfur/chlorine compounds in the gaseous, molten, and solid phase around the metal surface.

This leads to Type I hot corrosion (cf. Prakash et al.^[61]) and the microstructure of the alloy shows the formation of sulfides/chlorides and a corresponding depletion of the reactive components. As main corrosion mechanism in sintering plants for the iron and steel production, oxychloridation above 700 °C takes place.

4. Conclusion

Based on the high temperature corrosion studies within this work, the following conclusions can be drawn:

- The corrosive environment in a sintering plant for pig iron production suffers from high temperature oxidation and molten salt corrosion at 900 °C with dominant corrosive species NaCl, KCl, Na₂SO₄, and K₂SO₄.
- Based on the calculations of the Gibbs free energy changes at 1200 K, oxychloridation of metals and their oxides takes place concomitant with sulfidation.
- Low alloyed steels do not provide an effective corrosion resistance, due to the formation of insufficiently stable oxide scales.
- The scale formation on Cr-rich steels tends to be the same for different microstructures. The inner oxide layer mainly consists of Cr- and Mn-rich Fe-oxide, the outer scale mainly consists of Fe-oxide with Mn and Ni (if present in the alloy). The diffusion layer mostly consists of Si-oxide with corrosive salts.

- Martensitic Cr-steels are too low alloyed for the use in such environment; the formed oxide scales are spongy and allow the migration of corrosive salts to the base metal at a high rate.
- Austenitic heat resistant steels also suffer from insufficient protection due to the formation of two different oxide scales (Fe–Ni and Fe–Cr richer oxide scales).
- Ferritic-carbide, Cr-rich steels can be seen as a good material withstanding such environment. The formed layers are mostly homogenous and show low porosity and the selective corrosive attack on the chromium carbides is in a decent range.
- For both, the austenitic and the ferritic-carbide steel a minimal amount of chromium is needed to stabilise the oxide scales. At higher level of alloying elements, such as Cr and Ni the oxidation increases again caused by increased presence of metal ions at the metal-oxide interface and the resulting increase of the oxychloridation cycle.

Acknowledgements

This work was funded by the Austrian COMET-Program (Project K2 XTribology, no. 849109) and carried out at the “Excellence Centre of Tribology” and the “Centre of Electrochemical Surface Technology (CEST GmbH). Authors are grateful to voestalpine Stahl Linz GmbH for active research cooperation.

Received: October 28, 2016; Revised: January 6, 2017

Keywords: high temperature corrosion; oxidation; pig iron production; sintering plant; steel

References

- [1] A. Vignes, *Extractive Metallurgy - Processing Operations and Routes*, John Wiley & Sons, Hoboken, USA 2011.
- [2] M. Geerdes, H. Toxopeus, C. van der Vliet, *Modern Blast Furnace Ironmaking*, IOS Press BV, Amsterdam, The Netherlands 2009.
- [3] R. Bürgel, H. J. Maier, T. Niendorf, *Handbuch Hochtemperatur-Werkstofftechnik*, Vieweg und Teubner, Wiesbaden, Germany 2011.
- [4] D. Young, *High Temperature Oxidation and Corrosion of Metals*, Elsevier, Oxford, UK 2008.
- [5] G. Y. Lai, *High Temperature Corrosion and Materials Applications*, ASM International, Materials Park, USA 2007.
- [6] N. Birks, G. H. Meier, F. S. Pettit, *Introduction to the High Temperature Oxidation of Metals*, Cambridge University Press, Cambridge, UK 2006.

- [7] M. A. Uusitalo, P. M. J. Vuoristo, T. A. Mäntylä, *Corr. Sci.* **2004**, *46*, 1311.
- [8] H. Fujikawa, N. Maruyama, *Corros. Sci.* **1989**, *120*, 301.
- [9] J. Priss, H. Rojacz, I. Klevtsov, A. Dedov, H. Winkelmann, E. Badisch, *Corros. Sci.* **2014**, *82*, 36.
- [10] H. Rojacz, M. Varga, H. Kerber, H. Winkelmann, *J. Mater. Proc. Technol.* **2014**, *241*, 1285.
- [11] M. Varga, H. Rojacz, H. Winkelmann, H. Mayer, E. Badisch, *Tribol. Int.* **2013**, *65*, 190.
- [12] A. Sikora, H. Rojacz, K. Adam, L. Krabac, M. Varga, G. Fafílek, in *Tribology in Industry and Research* (Eds: A. Pauschitz, F. Franek), Österreichische Tribologi- scheGesellschaft, Wiener Neustadt, Austria **2016**.
- [13] A. Galerie, in: *Shreir's Corrosion - Comprehensive Corrosion* (Eds: R. A. Cottis, M. J. Graham), Elsevier B. V., Amsterdam, The Netherlands **2010**.
- [14] B. A. Pint, in: *Developments in High Temperature Corrosion and Protection of Materials* (Eds: W. Gao, Z. Li), CRC Press, Boca Raton, USA **2008**.
- [15] A. Bautista, F. Velasco, J. Abenojar, *Corr. Sci.* **2003**, *45*, 1343.
- [16] G. Goyal, H. Singh, S. Prakash, *Appl. Surf. Sci.* **2008**, *254*, 6653.
- [17] K. Przybylski, G. J. Yurek, *Mater. Sci. Forum* **1989**, *43*, 1.
- [18] J. L. Smialek, J. Doychak, D. J. Gaydosh, *Oxid. Met.* **1990**, *4*, 259.
- [19] T. Kuppan, *Heat Exchanger Design Handbook*, Marcel Dekker Inc., New York, USA **2000**.
- [20] A. S. Khanna, *Introduction to High Temperature Oxidation and Corrosion*, ASM International, Materials Park, USA **2002**.
- [21] M. Spiegel, in: *Shreir's Corrosion - Comprehensive Corrosion* (Eds: R. A. Cottis, M. J. Graham), Elsevier B.V., Amsterdam, The Netherlands **2010**.
- [22] L. J. Korb, D. L. Olson, *ASM Handbook Volume 13: Corrosion*, ASM International, Materials Park, USA **1992**.
- [23] H. Rojacz, A. Zikin, C. Mozelt, H. Winkelmann, E. Badisch, *Surf. Coat. Technol.* **2013**, *222*, 90.
- [24] R. John, in: *Shreir's Corrosion - Comprehensive Corrosion* (Eds: R. A. Cottis, M. J. Graham), Elsevier B.V., Amsterdam, The Netherlands **2010**.
- [25] N. Otsuka, in: *Shreir's Corrosion - Comprehensive Corrosion* (Eds: R. A. Cottis, M. J. Graham), Elsevier B.V., Amsterdam, The Netherlands **2010**.
- [26] K. Sridharan, T. R. Allen, in: *Molten Salts Chemistry*, Elsevier B.V., Amsterdam, The Netherlands **2013**.
- [27] A. Zahs, M. Spiegel, H. J. Grabke, *Corros. Sci.* **2000**, *42*, 1093.
- [28] H. Rojacz, F. Birkelbach, L. Widder, M. Varga, under submission to *Wear* **2016**. in press: DOI: 10.1016/j.wear.2017.01.004
- [29] ASTM G1-03, *Standard Practice for Preparing, Cleaning, and Evaluating Corrosion Test Specimens*, American Society for Testing and Materials, West Conshohocken, USA **2001**.
- [30] H. Rojacz, G. Mozdzen, F. Weigel, M. Varga, *Mat. Char.* **2016**, *118*, 370.
- [31] P. Y. Hou, in: *Shreir's Corrosion - Comprehensive Corrosion*, (Eds: R. A. Cottis, M. J. Graham), Elsevier B.V., Amsterdam, The Netherlands **2010**.
- [32] D. J. Young, J. Zhang, C. Geers, M. Schütze, *Mater. Corros.* **2011**, *62*, 7.
- [33] H. J. Grabke, R. Krajak, J. C. Nava Paz, *Corros. Sci.* **1993**, *35*, 1141.
- [34] D. J. Young, in: *Shreir's Corrosion - Comprehensive Corrosion* (Eds: R. A. Cottis, M. J. Graham), Elsevier B.V., Amsterdam, The Netherlands **2010**.
- [35] R. A. Antunes, M. C. L. de Oliveira, *Corros. Sci.* **2013**, *76*, 6.
- [36] H. T. Ma, C. H. Zhou, L. Wang, *Corros. Sci.* **2009**, *51*, 1861.
- [37] V. Firouzdor, K. Sridharan, G. Cao, M. Anderson, T. R. Allen, *Corros. Sci.* **2013**, *69*, 281.
- [38] Y. Kawahara, *Corros. Sci.* **2002** *44*, 223.
- [39] M. Broström, S. Enestam, R. Backman, K. Mäkelä, *Fuel Process. Technol.* **2013**, *105*, 142.
- [40] H. P. Nielsen, L. L. Baxter, G. Sclippab, C. Morey, F. J. Frandsen, K. Dam-Johansen, *Fuel* **2000**, *79*, 131.
- [41] H. Kassman, J. Petterson, B-M. Steenari, L-E. Amand, *Fuel Process. Technol.* **2013**, *105*, 170.
- [42] M. Spiegel, R. Krein, in: *Dampferzeugerkorrosion 2011* (Eds: A. Eisenblätter, R. Stark, T. Zänßler), Saxonia Standortentwicklungs- und Verwaltungsgesellschaft mbH, Freiberg, Germany **2011**.
- [43] L. Wang, J. E. Hustad, O. Skreiberg, G. Skjevraak, M. Gronli, *Energy Proc.* **2012**, *20*, 29.
- [44] D. L. Perry, *Handbook of inorganic compounds* CRC Press, Boca Raton, USA **2011**.
- [45] D. R. Lide, *Handbook of Chemistry and Physics* CRC Press, Boca Raton, USA **2007**.
- [46] S. D. Cramer, B. S. Covino, *ASM Handbook Volume 13 A - Corrosion: Fundamentals, Testing and Protection* ASM International, Materials Park, USA **2003**.
- [47] L. J. Korb, D. L. Olson, *ASM Handbook Volume 13- Corrosion, Testing and Protection*, ASM International, Materials Park, USA **1992**.
- [48] Y. Kawahara, K. Takakashi, Y. Nakagawa, T. Hosoda, T. Mizuko, in: *Proceedings - Corrosion 2000*, NACE International, Orlando, USA **2000**.
- [49] X. Gaus-Liu, *High-Temperature Chlorine Corrosion during Co-Utilisation of Coal with Biomass or Waste*, Cuvillier Verlag, Göttingen, Germany **2008**.
- [50] Y. Kawahara, *Corros. Eng.* **2005**, *54*, 213.
- [51] C.-C. Tsaur, J. C. Rock, C.-J. Wang, Y.-H. Su, *Mater. Chem. Phys.* **2005**, *89*, 445.
- [52] Y. Shinata, Y. Nashi, *Oxid. Met.* **1986**, *26*, 201.
- [53] Y. S. Li, M. Spiegel, S. Shimada, *Chem. Phys.* **2005**, *93*, 217.
- [54] N. Hiramatsu, Y. Uematsu, T. Tanaka, M. Kinugasa, *Mater. Sci. Eng. A* **1989**, *120*, 319.
- [55] F. Wang, Y. Shu, *Oxid. Met.* **2003**, *59*, 201.
- [56] Y. S. Li, Y. Niu, W. T. Wu, *Mater. Sci. Eng. A* **2003**, *345*, 64.

- [57] I. Barin, G. Platzki, *Thermochemical data of pure substances*, Wiley VCH Verlagsgesellschaft mbH Weinheim, Germany **1995**.
- [58] W. Gao, Z. Li, *Developments in High Temperature Corrosion and Protection of Materials* CRC Press, Boca Raton, USA **2008**.
- [59] H. T. Ma, C. H. Zhou, L. Wang, *Corros. Sci.* **2009**, *51*, 1861.
- [60] M. Fukumoto, C. Tachikawame, Y. Matsuzaka, M. Hara, *Corros. Sci.* **2012**, *56*, 105.
- [61] S. Prakash, in: *Developments in high-temperature corrosion and protection of materials*. (Eds: W. Gao) CRC Press, Boca Raton, USA **2008**.